
Since January 2020 Elsevier has created a COVID-19 resource centre with free information in English and Mandarin on the novel coronavirus COVID-19. The COVID-19 resource centre is hosted on Elsevier Connect, the company's public news and information website.

Computers in Biology and Medicine 135 (2021) 104591

Contents lists available at ScienceDirect

Computers in Biology and Medicine

journal homepage: www.elsevier.com/locate/compbiomed

# *In silico* analysis of RNA-dependent RNA polymerase of the SARS-CoV-2 and therapeutic potential of existing antiviral drugs

Sunil Kanti Mondal [a,1,*], Samyabrata Mukhoty [a,1], Himangsu Kundu [a], Subhajit Ghosh [a], Madhab Kumar Sen [b], Suvankar Das [c], Simone Brogi [d,*]

[a] Department of Biotechnology, The University of Burdwan, Burdwan, 713104, West Bengal, India
[b] Department of Agroecology and Crop Production, Faculty of Agrobiology, Food and Natural Resources, Czech University of Life Sciences Prague, Prague, Czech Republic
[c] Department of Genetics, University of Calcutta, 35 Ballygunge Circular Road, Kolkata, 700019, India
[d] Department of Pharmacy, University of Pisa, Via Bonanno 6, 56126, Pisa, Italy

ARTICLE INFO

*Keywords:*
SARS-CoV-2
RdRp
Computational biology
Molecular modelling
Remdesivir
Sofosbuvir

ABSTRACT

The continued sustained threat of the SARS-CoV-2 virus world-wide, urgently calls for far-reaching effective therapeutic strategies for treating this emerging infection. Accordingly, this study explores mode of action and therapeutic potential of existing antiviral drugs. Multiple sequence alignment and phylogenetic analyses indicate that the RNA-dependent RNA polymerase (RdRp) of SARS-CoV-2 was mutable and similar to bat coronavirus RaTG13. Successive interactions between RdRp (nsp12 alone or in complex with cofactors nsp7-8) and viral RNA demonstrated that the binding affinity values remained the same, but the sites of interaction of RdRp (highly conserved for homologous sequences from different organisms) were altered in the presence of selected antiviral drugs such as Remdesivir, and Sofosbuvir. The antiviral drug Sofosbuvir reduced the number of hydrogen bonds formed between RdRp and RNA. Remdesivir bound more tightly to viral RNA than viral RdRp alone or the nsp12-7-8 hexadecameric complex, resulting in a significant number of hydrogen bonds being formed in the uracil-rich region. The interaction between nsp12-7-8 complex and RNA was mediated by specific interaction sites of nsp7-8. Therefore, the conserved nature of RdRp interaction sites, and alterations due to drug intervention indicate the therapeutic potential of the selected drugs. In this article, we provide additional focus on the interacting amino acids of the nsp7-8 complex and highlight crucial regions that could be targeted for precluding a correct recognition of subunits involved in the hexadecameric assembly, to rationally design molecules endowed with a significant antiviral profile.

## 1. Introduction

Since its outbreak in December 2019, in Wuhan (Hubei Province in China), Severe Acute Respiratory Syndrome Coronavirus-2 (SARS-CoV-2 also known as 2019 novel coronavirus) has infected more than 150 million people and resulted in more than 3 million deaths across the globe (source: https://www.worldometers.info/coronavirus/). Fever, chills, and shortness of breath are the most common symptoms of SARS-CoV-2, while the lungs are the most affected organ. Additionally, there is a certain level of pathophysiological severity associated with conditions such as pneumonia and thrombosis [1–6].

SARS-CoV-2 belongs to a group of positive-sense ssRNA, enveloped viruses (60 nm–140 nm diameter), known as Coronaviruses. They acquired this name due to the presence of characteristic crown-like projections on their surfaces [7–9]. At present, only four families of these viruses have been identified, namely, α, β, γ, and δ. Among the human coronaviruses SARS-CoV and MERS-CoV fall in category β [10–13]. The SARS-CoV-2 genome contains 14 functional open reading frames (ORFs) including replicase and protease genes, as well as spike (S), envelope (E), membrane (M), and nucleocapsid (N) genes (order of appearance: 5′–3′) [10,14]. Replicase (ORF1a) and protease (ORF1b) genes can encode polyprotein1a (pp1a) and polyprotein1ab (pp1ab), which get further processed by Papain-like protease ($PL^{pro}$) and Chymotrypsin-like protease ($3CL^{pro}$) to yield sixteen individual non-structural proteins (nsp) [10,15]. Crucial to the coronavirus infection, trimeric spike glycoprotein (S protein) neutralizes antibodies,

* Corresponding author.
*E-mail addresses:* skmondal@biotech.buruniv.ac.in (S.K. Mondal), simone.brogi@unipi.it (S. Brogi).
[1] authors contributed equally to this work.

https://doi.org/10.1016/j.compbiomed.2021.104591
Received 25 January 2021; Received in revised form 17 June 2021; Accepted 17 June 2021
Available online 23 June 2021

binds to the host cell surface, mediates membrane fusion, and finally, the viral particles enter the host cells. The *N*-terminal or *C*-terminal domain of the S protein can serve as the receptor-binding domain, depending on the type of virus. Most coronaviruses use their *C*-terminal domain to bind to receptors [16,17]. SARS-CoV-2 has used the human angiotensin-converting enzyme 2 (*h*ACE2) as a receptor to enter human cells [18]. As a result, *h*ACE2 was also suggested as a potential drug target for developing anti-CoVid-19 agents [19]. However, the replication of viral RNA within host human cells is catalyzed by a special class of enzymes known as RNA-dependent RNA polymerase (RdRp or RNA replicase). Although, in general, RdRps share structural similarities with DNA-dependent DNA polymerases (DdDps) and reverse transcriptases, the error rate during the transcription process is higher. This higher error rate leads to genomic variations within the viral populations. Because of the process of RNA recombination, viruses can repair these mutations to acquire new genes or functions and result in selective benefits to the viral population [20]. CoVs replication and transcription processes are primarily facilitated by a set of non-structural proteins (products of viral polyproteins cleavage) and the RdRp. Non-structural proteins 7 and 8 (nsp7 and nsp8) act as cofactors for the SARS-CoV-2-RdRp (also known as nsp12) and play an important role in the replication and transcription cycle of these viruses [21]. In brief, the structure of the SARS-CoV-2-RdRp consists of a polymerase domain (RdRp domain) and a unique *N*-terminal domain that forms architecture similar to nidovirus RdRp-associated nucleotidyltransferase (NiRAN) [22,23]. In addition to this conformation, a cryo-EM map reveals that an interface domain connects the polymerase domain with the NiRAN domain. Further details regarding the structure of SARS-CoV-2-RdRp are available in the article by Gao and colleagues [24]. Several epidemiological studies describe the molecular pathogenesis of SARS-CoV-2 [10, 24–26].

The alarming increase in the number of SARS-CoV-2 cases worldwide, urgently calls for effective and life-saving strategies, including effective vaccines and drugs for treating emerging and re-emerging diseases. This study examined the potential of existing antiviral drugs to be used as therapeutics and to acquire information about their mode of action. Furthermore, this work delineates the effects of selected existing antiviral drugs on the interaction between RdRp and RNA of SARS-CoV-2 in the presence or absence of the cofactor nsp7-8 hexadecameric complex. We chose the drugs based on the previous available reports on the polymerase protein of several different RNA viruses, in which these antiviral drugs were found to be effective. However, this work is one of the first reports that considers the nsp12-7-8 hexadecameric complex by investigating its role in the presence of potential antiviral drugs. The systematic study reveals the conserved nature of the interaction sites of RdRp, and the alteration of these sites in presence of the selected antiviral drugs, proving their therapeutic potential. The identified interaction sites of cofactors can be further explored for designing effective drugs against SARS-CoV-2.

## 2. Materials and methods

All links enclosed in the manuscript were accessed on 03rd May 2020.

### 2.1. Retrieval of the sequences

The database from Zhang Lab (available online https://zhanglab.ccmb.med.umich.edu/COVID-19/) was examined to identify the amino acid sequence of RdRp of SARS-CoV-2. After that, its homologous sequences were retrieved using the online tool BLASTP 2.2.32 (https://blast.ncbi.nlm.nih.gov/Blast.cgi) [27]. In total, ORF1ab polyprotein from SARS-CoV-2 and 28 organisms (selection criteria: E-value $< 0.01$, in BLASTP search) were selected for further analyses. The 28 strains are selected on the basis of E-value. E-value meaning changes in the equivalent position due to chance only. The phylogenetic tree was generated by randomly bootstrapping the best E-value.

### 2.2. Multiple sequence alignment and phylogenetic analysis

The identification of the corresponding homologous regions among many input sequences revealed biological relationships among the sequences of interest. The sequence alignment profile of the selected sequences was performed using Clustal Omega tool (https://www.ebi.ac.uk/Tools/msa/clustalo/). JalVeiw option was used to obtain a well-defined representation of the sequence logos [28,29]. In addition to the sequence alignment, MEGAX (Molecular Evolutionary Genetic Analysis X) program was used to generate maximum-likelihood phylogenetic trees (bootstrap value: 1000; method: Jones-Taylor-Thornton (JTT) model) [30,31].

### 2.3. Molecular docking studies

Based on the previously published literature, eight antiviral drug molecules were selected for this study. The selection included Ribavirin (CID: 37542), Tenofovir (CID: 464205), Sofosbuvir (CID: 45375808), IDX-184 (CID: 135565589), YAK (CID: 11492563), Setrobuvir (CID: 135565932), Remdesivir (CID: 121304016), and Galidesivir (CID: 10445549). These drug molecules were chosen based on their potential to affect the polymerase activity of RdRp through inhibition/blocking of the catalytic domain, which is responsible for the binding with the viral RNA [32,33]. Data of each drug were retrieved from PubChem (https://pubchem.ncbi.nlm.nih.gov/). Drugs were treated by LigPrep (Schrödinger Release-2018) to obtain the starting structures for further computational studies. This application can generate the most probable ionization state for each input structure at the cellular pH value ($7.4 \pm 0.5$) using Epik tool. Moreover, the OPLS-AA_2005 force field was used for optimization, producing the lowest energy conformer for each ligand [34,35].

The SARS-CoV-2 repository of SWISS-MODEL (https://swissmodel.expasy.org/repository/species/2697049) was explored to obtain the structures of RdRp (https://swissmodel.expasy.org/interactive/JDUya4/models/02) and nsp7/nsp8 hetero-oligomeric complex (https://swissmodel.expasy.org/interactive/JhWqVj/models/01). The best model for RdRp structure was chosen based on the sequence similarity with its template (SMTL ID: 6m71.1). The application Protein Preparation Wizard implemented in Maestro (Schrödinger Release-2018) was used for treating the proteins to obtain reasonable starting structures for further computational analysis as previously reported [36–38]. Furthermore, MolProbity was employed to assess the quality of the secondary structure, including phi/psi dihedral angles, of each subunit composing the hexadecameric complex [39], before starting the assembly of the mentioned arrangement. The analysis revealed that the residues of proteins were in the allowed regions, with no residues in the disallowed regions (Figure S1-S3, for nsp7, nsp8, and nsp12, respectively). All residues of the refined subunits reside in acceptable regions of the Ramachandran plot. This value was more than the cut-off value (96.1%) defined for the most reliable models [40]. Consequently, protein quality was satisfactory, and they could be used for further computational studies. Molecular docking studies were conducted through HDOCK web-server (http://hdock.phys.hust.edu.cn/) [41]. The server performed protein-protein and protein-DNA/RNA docking automatically and can predict interactions by employing a hybrid algorithm of template-based and template-free docking. Possible binding sites were not specified, resulting in a blind docking calculation. For accomplishing all docking calculations in this study (blind docking, protein-protein docking, and RNA-protein docking), we used the same program, HDOCK web-server, to treat all components of a given system in the same way, limiting the uncertain. In particular, HDOCK server works in a four-step manner. This server can predict the binding complexes between two molecules (e.g. proteins and nucleic acids) by using a hybrid docking strategy. After the data input for receptor/ligand molecules, a sequence similarity search was conducted against the PDB sequence database in search of the homologous sequences for both the

receptor and ligand molecules. The HHSuite package was used to find the homologous sequence for an input protein and the FASTA program was used for nucleic acids. This yielded two sets of homologous templates, one for the receptor and another for the ligand molecule. Next, the two sets of the templates obtained were compared to check whether they have common records with the same PDB codes. If such PDB codes were found, the server selected a common template for both the receptor and the ligand molecules. However, if multiple templates were available, the server selected the template with the highest sequence convergence, the highest sequence similarity and with the highest resolution. Then, models were built with the selected templates by using MODELLER (https://salilab.org/modeller/), in which the sequence alignment was conducted using ClustalW. For the docking process, a fast Fourier transform (FFT)-based docking program was used to calculate the interaction energy of two rigid macro-molecular bodies as a sum of correlation functions and then evaluate the putative interactions on a grid. The improved shape-based pairwise scoring function was used. The score for a ligand grid was based on the contribution from its nearest receptor grids and from the other receptor grids, with an angle interval of 15° for rotational sampling, using a spacing of 1.2 Å in this FFT-based method. The ranked binding modes were clustered with a root-mean-square deviation (RMSD) cut off of 5 Å. The RMSD was calculated using backbone atoms. Between two binding modes having a ligand RMSD lower or equal to 5 Å, the one with the better score was considered. For the protein-nucleic acid docking, there were around 4392 evenly distributed rotations in the Euler space and, therefore, 4392 binding solutions for a single docking run for the user. Final binding models were generated from the top 100 binding models.

The receptor-ligand contacts were identified through UCSF Chimera (https://www.cgl.ucsf.edu/chimera/), LigPlot + tool [42] and Protein-Ligand Interaction Profiler (https://projects.biotec.tu-dresden.de/plip-web/plip/index) [43,44]. PyMOL software (The PyMOL Molecular Graphics System, version 1.8.4.0, Schrödinger, LLC, New York, 2018) and UCSF Chimera were used to generate all pictures in this work.

### 2.4. Molecular dynamics simulations

Molecular dynamics (MD) simulations were performed using Desmond software (Desmond 5.6 academic version, D. E. Shaw Research "DESRES"), employing Maestro as graphical interface (Desmond Molecular Dynamics System, version 5.6, D. E. Shaw Research, New York, NY, 2018. Maestro-Desmond Interoperability Tools, Schrödinger, New York, NY, 2018). MD was performed using the Compute Unified Device Architecture (CUDA) API [45] on two NVIDIA GPUs. First, the complexes derived from docking studies were imported in Maestro and Desmond system builder solvated the complexes into a cubic box filled with water, simulated by TIP3P model [38,46]. OPLS force field [47] was used for MD calculations. OPLS-aa (all atom) included every atom explicitly with specific functional groups and types of molecules, including several bio-macromolecules [36,38,48,49]. $Na^+$ and $Cl^-$ ions were added to provide a final salt concentration of 0.15 M to simulate physiological concentration of monovalent ions. Constant temperature (300 K) and pressure (1.01325 bar) was employed with the NPT (constant number of particles, pressure and temperature) as an ensemble class. RESPA integrator [50] was used for integrating the equations of motion, with an inner time step of 2.0 fs for bonded and non-bonded interactions within the short-range cutoff. Nose-Hoover thermostats [51] were employed for keeping a constant simulation temperature, and the Martyna-Tobias-Klein method [52] was used to control the pressure. Long-range electrostatic interactions were calculated by particle-mesh Ewald method (PME) [53]. The cutoff for van der Waals and short-range electrostatic interactions was set at 9.0 Å. The equilibration of the system was performed using the default protocol provided in Desmond, which consisted of a series of restrained minimization and MD simulations used to slowly relax the system. Consequently, one individual trajectory for each complex of 100 ns was calculated. The trajectory files were analyzed using the tools implemented in the Desmond package. The same application was used to generate all plots concerning MD simulations performed in this study. Accordingly, the RMSD was calculated using the following equation:

$$RMSD_x = \sqrt{\frac{1}{N}\sum_{i=1}^{N}\left(r_i'(t_x) - r_i(t_{ref})\right)^2}$$

where the $RMSD_x$ is referred to the calculation for a frame x, N is the number of atoms in the atom selection; $t_{ref}$ is the reference time, (typically the first frame is used as the reference and it is regarded as time t = 0); and r' is the position of the selected atoms in frame x, after superimposing on the reference frame, where frame x is recorded at time $t_x$. The procedure was repeated for every frame in the simulation trajectory. The following equation was used for the calculation of the root-mean-square fluctuation (RMSF):

$$RMSF_i = \sqrt{\frac{1}{T}\sum_{t=1}^{T}\langle\left(r_i'(t) - r_i(t_{ref})\right)^2\rangle}$$

where $RMSF_i$ is referred to a generic residue i, T is the trajectory time over which the RMSF is calculated, $t_{ref}$ is the reference time, $r_i$ is the position of residue i; r' is the position of atoms in residue i after superposition on the reference, and the angle brackets indicate that the average of the square distance is taken over the selection of atoms in the residue.

## 3. Results and discussion

### 3.1. Phylogenetic analysis

Viruses are incapable of self-maintenance and self-replication [54]. Rapid globalization in the 21st century has simultaneously forced pathogens to also adapt to new environments. Aggressive environmental threats have also left humans more exposed to wildlife (*e.g.* bat), compounding the chances of viral infections. Indeed, severe deforestation and other environmental pressures have increased threats to humans. Furthermore, even among concurrent strains, the evolution of host immune responses induced selective pressure, resulting in unbalanced survival abilities. These have broadened the field of "phylodynamics" research [55,56].

Phylogenetic and sequence alignment analyses were conducted to explore the relationships between the selected taxa. Longer branch length corresponds with greater mutations acquired by the organism. In all cases, a close relationship between the bat coronavirus RaTG13 and SARS-CoV-2 was observed. A similar relationship was also found by various researchers, leading to the conclusion that SARS-CoV-2 is genetically similar to RaTG13 (isolated from bat in Yunnan in 2013) [57,58]. Based on the whole-length phylogenetic tree of the polyprotein ORF1ab, SARS-CoV-2 was observed to be homologous to the coronavirus RaTG13 in bats. The branch length of the coronavirus RaTG13 is slightly longer than that of SARS-CoV-2; however, for other phylogenetic trees, the branches of RaTG13 coronavirus and SARS-CoV-2 were reversed (Fig. 1A–C). These findings support the conclusion that slightly more mutations were acquired in RaTG13 coronavirus in bats than in SARS-CoV-2 over the length of ORF1ab polyprotein.

The output of multiple sequence analysis showed the differences in amino acids at 12 diverse positions within the ORF1ab sequence (which corresponds to RdRp). At site 4495 (corresponding to the $90^{th}$ amino acid residue of RdRp), valine is the most frequently observed amino acid. However, in some cases, valine was replaced by leucine (bat_coronavirus_RaTG13/1–7095 and SARS-CoV-2) and some places by isoleucine. The substitution observed in both the cases was within the same amino acid group, *i.e.*, neutral and non-polar. The site 4497 (corresponding to the $92^{nd}$ amino acid residue of RdRp) was occupied by glutamate (negatively charged, polar and hydrophilic), except for bat_SARS-like_coronavirus/1–7092 in which the glutamate was replaced by

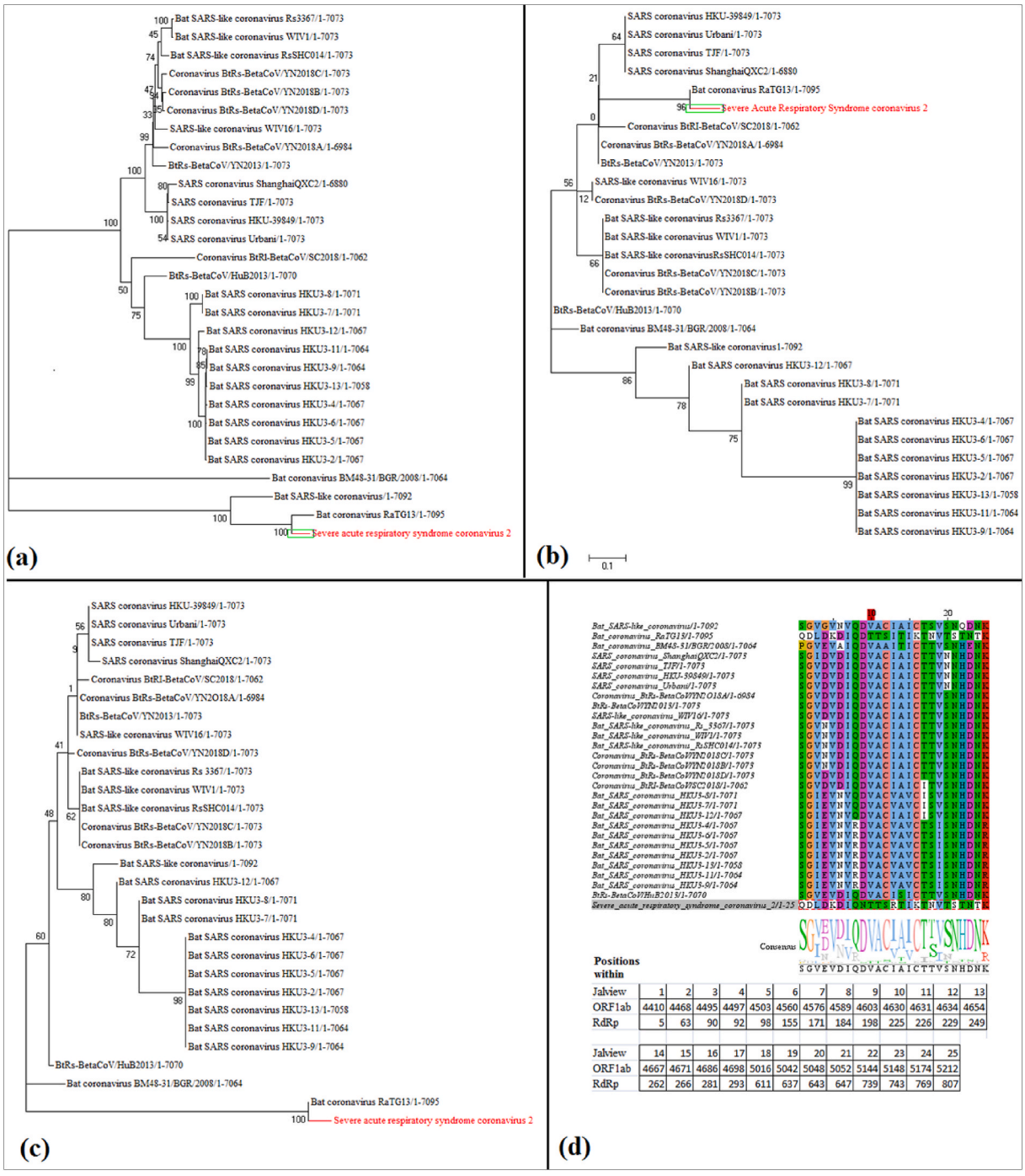


**Fig. 1.** Phylogenetic tree following maximum-likelihood method with 1000 bootstrap values considering (A) entire ORF1ab sequences and (B) 12 most mutable positions within RdRp; (C) observed 25 mutations (including 12 most mutable positions/sites: 3, 4, 6, 7, 8, 13, 15, 17, 18, 19, 20, 25 within JalView) within RdRp of SARS-CoV-2 and (D) JalView representation of multiple sequence alignment of ORF1ab for the 25 selective mutable positions within RdRp.

glycine (non-polar, aliphatic). In cases of bat_coronavirus_RaTG13/1–7095 and SARS-CoV-2, glutamate was replaced by aspartate. Both glutamate and aspartate are acidic amino acids. In some cases, glutamate was also substituted with asparagine, a neutral, nonpolar amino acid. With some exceptions, aspartic acid (anionic amino acid) and isoleucine (non-polar) populate sites 4560 (corresponding to the 155$^{th}$ amino acid of RdRp) and 4576 (corresponding to the 171$^{st}$ amino acid of RdRp). The site 4594 (corresponding to the 184$^{th}$ amino acid of RdRp) was occupied by glutamine (polar, uncharged), with some exceptions in some bat_SARS_coronaviruses in which it was replaced by a charged and polar amino acid residue, arginine. Sites 4564 (corresponding to the 249$^{th}$ amino acid of RdRp) and 4671 (corresponding to the 266$^{th}$ amino acid of RdRp) were mainly occupied by isoleucine (non-polar, aliphatic), with some exceptions. Sites 4698 (corresponding to the 293$^{rd}$ amino acid of RdRp), 5016 (corresponding to the 611$^{th}$ amino acid of RdRp), 5042 (corresponding to the 637$^{th}$ amino acid of RdRp), 5048 (corresponding to the 643$^{rd}$ amino acid of RdRp) and 5212 (corresponding to the 804$^{th}$ amino acid of RdRp) were predominantly occupied by threonine, valine, serine, and lysine, respectively, with some exceptions. A detailed analysis of these sites is provided in Fig. 1.

Furthermore, out of the twenty-five mutations observed, along the length of the RdRp, seventeen of these mutations were observed outside

the polymerase domain of RdRp and belong to the NiRAN domain. For all seventeen mutations, SARS-CoV-2 and bat coronavirus RaTG13 have identical amino acids at all equivalent positions except for position 4603 and 4654 of the ORF1ab polyprotein, corresponding to positions 198 and 249 of RdRp, respectively. Accordingly, these two organisms show striking differences in amino acid sequence concerning the other taxa. At position 198 of RdRp, a change in aspartic acid to asparagine was observed between bat coronavirus RaTG13 and SARS-CoV-2. In addition, at position 249, an isoleucine (bat coronavirus RaTG13) was replaced by an arginine (SARS-CoV-2) (Fig. 1B–D). All mutable positions in the polymerase domain of RdRp presented identical amino acids at equivalent positions for both organisms. By comparing all of the twenty-five positions between SARS-CoV-2 and other SARS-CoVs (SARS coronavirus Shanghai QXC2, SARS coronavirus TJF, SARS coronavirus HKU and SARS coronavirus Urbani) it is possible to observe that, SARS-CoV-2 shows similarities in the amino acid sequence with the SARS counterparts, mainly in the conserved NiRAN domain. The main changes were observed at the following positions: Asp4497 (corresponding to the position 92 of RdRp), Asp4560 (corresponding to the position 155 of RdRp), Ile4576 (corresponding to the position 171 of RdRp), Gln4589 (corresponding to the position 184 of RdRp), Ile4671 (corresponding to the position 266 of RdRp), and Thr4698 (corresponding to the position 293 of RdRp). However, between SARS-CoV-2 and the SARS counterparts within the variable polymerase two of eight identical amino acid substitutions were found within the polymerase domain: Val5042 (corresponding to the position 637 of RdRp) and Lys5212 (corresponding to the position 807 of RdRp).

Based on phylogenetic analysis established on the full length of ORF1ab or only on the mutable sites and only considering this evolutionary frame, it is evident that SARS-CoV-2 is related to bat coronavirus RaTG13. The total number of acquired mutations in bat coronavirus RaTG13 is slightly higher than SARS-CoV-2, according to the branch length of full length of ORF1ab phylogenetic tree. The occurrence of identical amino acids in the equivalent mutable positions along the entire length of ORF1ab between bat coronavirus RaTG13 and SARS-CoV-2 reflects evolutionary relatedness among these two taxa.

When twenty-five mutable positions along the length of ORF1ab corresponding to viral RdRp were considered, SARS-CoV-2 acquired the most mutations, despite the evolutionary relationship between bat coronavirus RaTG13 and SARS-CoV-2 remaining unchanged (Fig. 2). Furthermore, these observed mutations along the length of RdRp, as well as amino acid changes within the NiRAN domain (1–397 amino acid sequence) of RdRp, indicate that all equivalent positions in SARS-CoV-2 and bat coronavirus RaTG13 are occupied by identical amino acids with only two exceptions of ORF1ab polyprotein, which correspond to positions 198 and 249 of RdRp. A change in aspartic acid to asparagine was found in position 198 of RdRp in SARS-CoV-2. While the change from aspartic acid to asparagine can improve the possibility to form hydrogen bonds with its ligand, the change from isoleucine to arginine in position 249 of SARS-CoV-2 RdRp can form salt bridge contacts more efficiently during binding to any ligand. Furthermore, during the evolution of SARS-CoV-2, several remarkable substitutions occur within the NiRAN domain of the RdRp in contrast to the SARS counterparts. In fact, compared to SARS-CoV-2 RdRp, some nonpolar amino acids of SARS counterparts RdRp have been replaced by a negative amino acid at position 63, positive amino acids at positions 98 and 249, and polar amino acids at positions 225, 226, and 262. As a result, the SARS-CoV-2 RdRp eventually encloses more polar amino acids useful for forming hydrogen bonds, and this event has implications for the design of small-molecules targeting the aforementioned-specific residues. This aspect can be relevant to improve binding affinity and selectivity against SARS-CoV-2 RdRp over its counterpart in related viruses. The equivalent positions present in the length of ORF1ab corresponding to the polymerase domain of RdRp are quite large, but the amino acid differences between SARS-CoV-2 and the other SARS counterparts are found in critical positions of RdRp (e.g. Val637 and Lys807). Additionally, in SARS-CoV-2 at position 5148 of ORF1ab (corresponding to the position 743 of RdRp), the substitution of aspartic acid with asparagine reflects the fact that the asparagine is more efficient at forming hydrogen bonds with any ligand. This aspect is also relevant for improving the efficacy and selectivity of rationally designed ligands. These notable amino acid changes, along with the higher number of acquired mutations in SARS-CoV-2 RdRp are the main reasons for the evolutionary divergence between SARS-CoV-2 and the SARS counterparts. More importantly, the observed amino acid changes in the polymerase domain of SARS-CoV-2 RdRp can be the cause for its increased

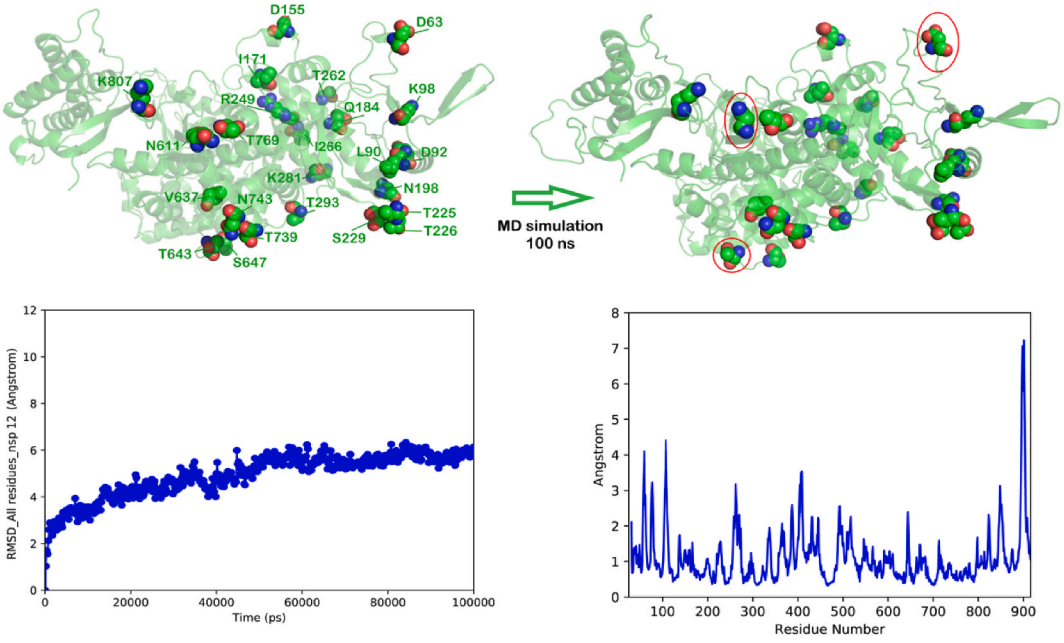


**Fig. 2.** Schematic representation of mutable positions and their behavior during 100 ns of MD simulation of nsp12. RMSD and RMSF of the system throughout the simulation are also reported. Mutable residues involved in relevant conformational changes are highlighted by a red circle. All hydrogen atoms were omitted for the sake of clarity.

efficiency.

For reporting a comprehensive view of mutable positions, we performed a MD simulation of nsp12 for investigating the behavior of mutable residues. The output of this calculation is reported in Fig. 2. In particular, we observed a general stability of the system with small fluctuations, as highlighted by calculating RMSD and RMSF. As previously experienced, we observed protein fluctuation at the boundaries of the sequence. In fact, we detected main fluctuations in the last 20 amino acid residues of nsp12, while minor movements were detected for the first portion of the protein. Observing the MD simulation trajectory, we noted that mutable positions were not involved in relevant conformational changes, with some exceptions, which belong to the region with minor fluctuations: Asp63, Thr643, and Asn611. Only minor conformational changes were observed in these residues.

### 3.2. Molecular docking and molecular dynamics studies

The current study aimed to identify the interacting sites of RdRp or its complex with viral RNA, as well as the behavior of RdRp in presence of antiviral drugs. To achieve this goal, we conducted multiple molecular docking studies with SARS-CoV-2-nsp12. The activity of SARS-CoV-2-nsp12 polymerase is stimulated by nsp7 and nsp8. To mimic the *in vivo* situation, molecular docking calculations were performed to investigate the RdRp activity of SARS-CoV-2-nsp12 using a complex containing nsp7 and nsp8 in a hexadecameric arrangement. Our findings revealed that the RNA has a higher affinity for the nsp7 and nsp8 complexes than for SARS-CoV-2-nsp12 within the SARS-CoV-2-nsp7-8-12 complex. According to previous reports, nsp7 participates in the polymerase activity, and nsp8 has a non-canonical RdRp activity [59,60]. These findings imply that nsp7 and nsp8 in this complex must contain an RNA binding domain. The ribonucleotides (NTPs) entrance channel within the nsp12 (formed by the basic residues such as Lys545, Arg553, and Arg555 from Motif F), facilitate the entry of incoming NTPs [61]. After the initial binding of the template or parental RNA with nsp7, the RNA is expected to mediate its entry into the active site of the nsp12 polymerase domain (formed by Motifs A and C) and form a new RNA strand [22]. Furthermore, the nsp7/nsp8 complex interacts with nsp12, targeting the following residues located in the polymerase domain: Thr409, Lys411, Trp509, Gly510, Arg513, Gly897, and Met899. Additionally, Asn104 and Asn136 of nsp8 (from the hexadecameric structure nsp7/nsp8) form two hydrogen bonds with nsp12 targeting Trp509 and Thr409 (Fig. 3 and Figure S4, Table 1).

For improving the reliability of the docking calculation, we investigated the dynamics of the system by performing a MD simulation study. The nsp12 was subjected to a simulation of 100 ns to better understand the behavior of interacting residues. The outcome of this computational investigation (Figure S4) highlighted a general stability of the system indicated by calculating RMSD and RMSF (also visible in Fig. 2). Furthermore, 100 ns of simulation of the system did not alter the interface exposure, and the identified interacting residues (Table 1) can still interact with nsp7 and nsp8 since no relevant conformational changes were observed in this interacting domain. This event is confirmed by a further docking calculation achieving the assembly of the nsp12 with nsp7 and nsp8. The calculation output using the structure of nsp12 after 100 ns as a starting point, is comparable to that reported in Fig. 2B with only minor changes in interaction sites (Figure S4). The main residues of nsp12, driving the recognition between the latter and its cofactors, were confirmed to establish the main contacts with nsp7 and nsp8. We observed only few additional contacts stabilizing the binding mode. Indeed, Lys411 is involved in a H-bond with Asp134 (nsp8), while Thr409 can establish an additional H-bond with Asn140 (nsp8). Finally, we observed that Lys508 can further stabilize the contacts of the loop by interacting with Asp99 (nsp8) (Figure S4).

Therefore, the nsp7/nsp8 complex might also occupy the nsp12 polymerase domain, making potential drug-binding (functional) sites located in the viral polymerase domain inaccessible to many drugs, precluding a strong inhibition of enzyme function or an interference in complex formation. The binding affinity (Fig. 4) of only nsp12 to RNA is slightly better (−328.84 kcal/mol with an RMSD value of 133.19 Å)

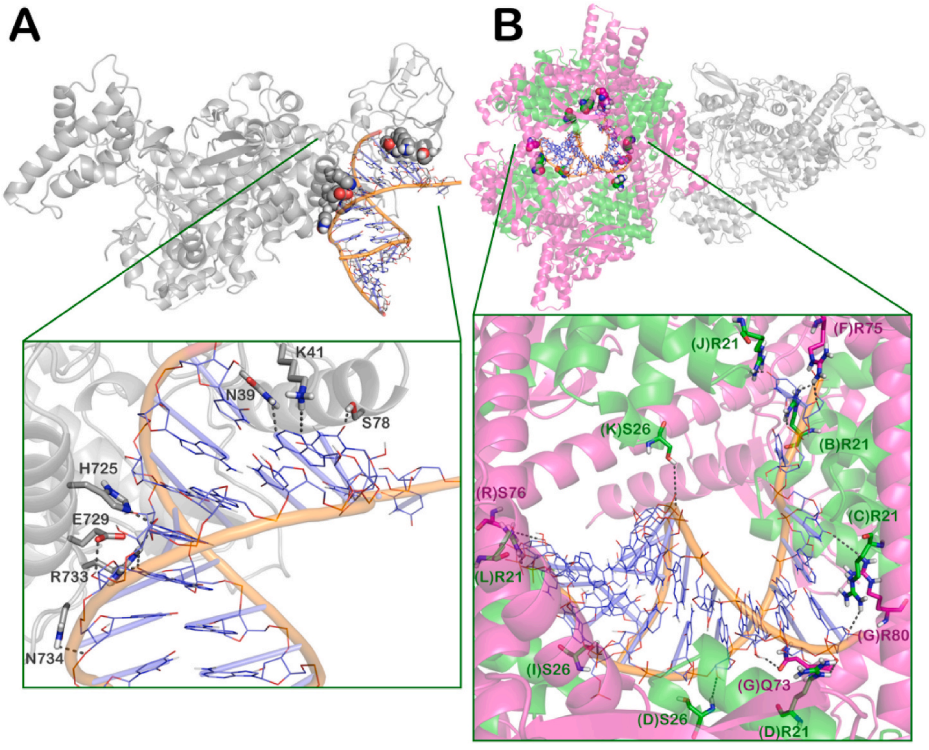


**Fig. 3.** Molecular interactions between (A) nsp12 (gray) and RNA and (B) nsp7-8-12 (green, magenta, and gray, respectively) complex and viral RNA. Interacting residues are represented by sticks and labelled (the corresponding chain of each interacting residue is reported between brackets). H-bonds are represented by gray-dotted lines. The picture was generated by PyMOL software (The PyMOL Molecular Graphics System, v1.8; Schrödinger, LLC, New York, 2015).

**Table 1**
Interactions among the hexadecameric complex formed by nsp12 and nsp7/nsp8 of SARS-CoV-2 as obtained from UCSF Chimera software. The distance is referred to the distance between the centroid of the selected residues. The bond length (Å) is defined as the distance between the atoms involved in the hydrogen bonding.

| nsp12 | nsp7-8 | Type of contact | Overlap | Distance | Bond length |
|---|---|---|---|---|---|
| Gly897 | Asn69 (nsp7) | non-polar | 1.932 | 1.368 | – |
| Gly510 | Cys72 (nsp7) | non-polar | 1.165 | 2.135 | – |
| Met899 | Arg111 (nsp8) | non-polar | 1.002 | 2.518 | – |
| Trp509 | Arg96 (nsp8) | non-polar | 0.742 | 3.018 | – |
| Leu900 | Arg111 (nsp8) | non-polar | 0.727 | 3.033 | – |
| Thr409 | Met174 (nsp8) | non-polar | 0.718 | 3.042 | – |
| Lys411 | Asn136 (nsp8) | non-polar | 0.654 | 2.866 | – |
| Arg513 | Glu73 (nsp7) | non-polar | 0.641 | 2.659 | – |
| Thr409 | Asn136 (nsp8) | polar | – | – | 2.767 |
| Trp509 | Asn104 (nsp8) | polar | – | – | 2.681 |

than that of the nsp7-8-12 complex with the same RNA template (−317.09 kcal/mol with an RMSD value of 83.68 Å), but the lower RMSD value indicates that the nsp7-8-12 complex has better confirmation to efficiently interact with the viral RNA. Here, the RMSD was calculated considering the complex protein(s) (nsp12 or nsp7-8-12) and ligand (template RNA). This trend is also confirmed using the structure of nsp12 after 100 ns of MD simulation as a starting point.

We have observed that nsp12 interacts with the viral RNA (Fig. 3) typically by forming hydrogen bonds with it. Certain residues are important in this interaction. In particular, two polar, uncharged amino acids, asparagine (positions 39 and 734 within nsp12) and serine (position 78 of nsp12) are involved in the formation of three hydrogen bonds. The acidic amino acid glutamic acid (position 729 of nsp12) can interact with the viral RNA by establishing one hydrogen bond. Furthermore, some basic amino acids such as lysine (position 41 of nsp12), histidine (position 725 of nsp12), and arginine (position 733 of nsp12) H-bind the viral RNA before the inclusion of drug molecules (Table 2).

When we analyzed the interaction between nsp12 and viral RNA after the incorporation of drug molecules with the nsp12 prior to viral RNA binding, interacting amino acids were altered; although the binding affinity between nsp12 and the viral RNA was not significantly altered. Another striking observation is that, while different drugs interact with different amino acid residues of nsp12 (Supplementary Table 1), with few exceptions, nsp12 interacts with the template RNA through identical residues (Asp499, Tyr521, Ser814, Ser861, and Tyr903). A further interacting residue (Gln492) was observed for nsp12 complexed with Ribavirin. In contrast, Setrobuvir interacted with nsp12 by establishing hydrogen bonds targeting Tyr38, Asp40, Ser78, Asn79, Gly220, Asn722, and Asn734 (Table 1). As a result, it is possible to conclude that the drug Setrobuvir had not effect on the interaction of nsp12 and viral RNA. This means that it can no longer be considered a potential viral RdRp inhibitor. In contrast, when Sofosbuvir was added to nsp12 prior to RNA binding, the total number of amino acids involved in the interaction with viral RNA decreased. Based on these observations, it is possible to conclude that, Sofosbuvir can effectively act as a potential RdRp inhibitor.

Subsequent molecular docking calculation was performed on nsp12 bound with its cofactors nsp7 and nsp8, in hexadecameric structure. The goal of this docking study was to identify the amino acid residues of the nsp12-7-8 hexadecameric complex that interact with viral RNA. We observed that, rather than binding with nsp12, the template RNA established three H-bonds with the basic residues Arg21 and Lys27 of nsp7. Alternatively, the template RNA formed hydrogen bonds with the basic amino acid arginine located at positions 75 and 80 of nsp8 (Table 3).

It has also been observed that the nsp7-8 cofactors provide some level of protection to nsp12, preventing drugs from gaining access to viral RdRp. Although some of the interacting sites of nsp7-8-12 hexadecameric structure could be altered after the inclusion of the selected drugs into nsp12 (Figs. 5 and 6) and before its binding with the cofactors, the viral RNA could still bind nsp7-8 cofactors. An exception is represented by the nsp12 complexed with Sofosbuvir prior to the binding with the nsp7-8 cofactors. After the inclusion of Sofosbuvir into nsp12, which is then complexed with nsp7-8 in a hexadecameric structure, the total number of hydrogen bond-forming amino acids was reduced. Furthermore, rather than the nsp7-8 cofactors, the template RNA interacts with the acidic residue Asp499, aromatic residue Tyr521 and Tyr903, and with the polar uncharged residue Ser814 of nsp12. Sofosbuvir is also more effective in this instance, as the total number of interacting amino acids reduces and the interaction sites become drastically altered.

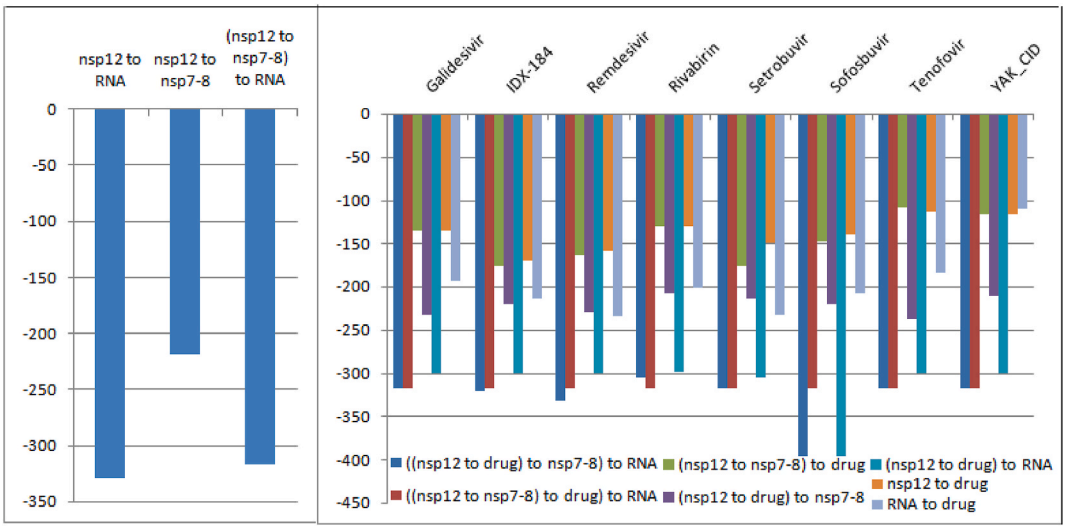


**Fig. 4.** Binding energy values (kcal/mol) obtained from HDOCK for different possible interactions among nsp12, nsp7-8 hexadecameric complex, drug, and RNA. More negative values indicate more efficient interactions.

**Table 2**
Interacting sites of RdRp (nsp12) involved in the interaction with viral RNA in the absence and presence of drugs as found by the computational approaches used in this study.

| nsp12/RNA | | nsp12/RNA in the presence of drugs | | | | | | | |
|---|---|---|---|---|---|---|---|---|---|
| | | IDX_184 | | Remdesivir | | Galidesivir | | Ribavirin | |
| Position | Residue | Position | Residue | Position | Residue | Position | Residue | Position | Residue |
| 39 | Asn | 499 | Asp | 499 | Asp | 499 | Asp | 492 | Gln |
| 41 | Lys | 521 | Tyr | 521 | Tyr | 521 | Tyr | 499 | Asp |
| 78 | Ser | 814 | Ser | 814 | Ser | 814 | Ser | 521 | Tyr |
| 725 | His | 861 | Ser | 861 | Ser | 861 | Ser | 814 | Ser |
| 729 | Glu | 903 | Tyr | 903 | Tyr | 903 | Tyr | 861 | Ser |
| 733 | Arg | | | | | | | 903 | Tyr |
| 734 | Asn | | | | | | | | |
| nsp12/RNA | | nsp12/RNA in the presence of drugs | | | | | | | |
| | | Setrobuvir | | Sofosbuvir | | Tenofovir | | YAK | |
| Position | Residue | Position | Residue | Position | Residue | Position | Residue | Position | Residue |
| 39 | Asn | 38 | Tyr | 499 | Asp | 499 | Asp | 499 | Asp |
| 41 | Lys | 40 | Asp | 521 | Tyr | 521 | Tyr | 521 | Tyr |
| 78 | Ser | 78 | Ser | 814 | Ser | 814 | Ser | 814 | Ser |
| 725 | His | 79 | Asn | 903 | Tyr | 861 | Ser | 861 | Ser |
| 729 | Glu | 220 | Gly | | | 903 | Tyr | 903 | Tyr |
| 733 | Arg | 722 | Asn | | | | | | |
| 734 | Asn | 734 | Asn | | | | | | |

**Table 3**
Interacting sites of the nsp12-7-8 complex involved in contacts with viral RNA in the absence and presence of drugs.

| (nsp12 to nsp7-8) to RNA | | (nsp12 to nsp7-8) with drug to RNA | | | | | | | |
|---|---|---|---|---|---|---|---|---|---|
| | | IDX_184 | | Remdesivir | | Ribavirin | | Sofosbuvir | |
| Position | Residue | Position | Residue | Position | Residue | Position | Residue | Position | Residue |
| 21 (nsp7) | Arg | 21 (nsp7) | Arg | 21 (nsp7) | Arg | 21 (nsp7) | Arg | 21 (nsp7) | Arg |
| 26 (nsp7) | Ser | 26 (nsp7) | Ser | 26 (nsp7) | Ser | 26 (nsp7) | Ser | 26 (nsp7) | Ser |
| 73 (nsp8) | Gln | 73 (nsp8) | Gln | 73 (nsp8) | Gln | 73 (nsp8) | Gln | 29 (nsp7) | Trp |
| 75 (nsp8) | Arg | 75 (nsp8) | Arg | 75 (nsp8) | Arg | 75 (nsp8) | Arg | 73 (nsp8) | Gln |
| 76 (nsp8) | Ser | 80 (nsp8) | Arg | 80 (nsp8) | Arg | 80 (nsp8) | Arg | 75 (nsp8) | Arg |
| 80 (nsp8) | Arg | | | | | | | 80 (nsp8) | Arg |
| nsp7-8 complex binds nsp12 on its *finger domain (L366-A581 and K621-G679) and thumb domain (H816-Q932)* [22] | | Galidesivir | | Setrobuvir | | Tenofovir | | YAK | |
| | | Position | Residue | Position | Residue | Position | Residue | Position | Residue |
| | | 21 (nsp7) | Arg | 21 (nsp7) | Arg | 21 (nsp7) | Arg | 21 (nsp7) | Arg |
| | | 26 (nsp7) | Ser | 26 (nsp7) | Ser | 26 (nsp7) | Ser | 26 (nsp7) | Ser |
| | | 73 (nsp8) | Gln | 73 (nsp8) | Gln | 73 (nsp8) | Gln | 73 (nsp8) | Gln |
| | | 75 (nsp8) | Arg | 75 (nsp8) | Arg | 75 (nsp8) | Arg | 75 (nsp8) | Arg |
| | | 80 (nsp8) | Arg | 80 (nsp8) | Arg | 80 (nsp8) | Arg | 80 (nsp8) | Arg |

In order to mimic the *in vivo* situation, we performed a series of molecular docking calculations with the nsp12-7-8 hexadecameric complex and each chosen drug. This calculation was useful to determine whether the hexadecameric complex residues responsible for viral RNA interactions had changed after the inclusion of the selected drugs. The viral RNA mostly maintained the interactions with nsp7/nsp8 cofactors of the nsp12-7-8 complex as detected considering the nsp12-7-8 complex and template RNA in the absence of drugs (Table 4).

Based on the above analysis, none of the selected drugs were effective because the interacting amino acid residues were only altered after incorporation of Sofosbuvir.

In order to validate the docking results, we further analyze each complex reported in Figs. 5 and 6 by MD simulation. This investigation allowed dynamic study of the behavior of proteins and their interactions, in the presence of drugs [36,62]. We evaluated the stability of the selected complexes (e.g. nsp7-8-12, viral RNA, and antiviral drugs) for better understanding the role of antiviral drugs against SARS-CoV-2 RdRp. We also investigated if the main contacts found by molecular docking calculations were conserved through the MD simulations, or if novel contacts arose from the dynamics of proteins until the formation of low-energy stable complexes. The output of MD simulations is illustrated in Fig. 7. This picture reported the calculation of RMSD that indicates the stability of a given complex.

The target protein showed reasonably stable structure lacking any major expansion/contraction, after the binding of these ligands throughout the simulation period. In Figures S5-S12 are reported details about the main contacts and the type of interaction found for each selected drug. Regarding IDX_184 (Figure S5), the main contacts (Supplementary Table 1) found by docking, were maintained (Thr817, Leu819, Tyr831, and His872), although we observed that the interaction with Tyr877 was lost and became sporadic. The IDX_184 could stabilize its binding by establishing relevant contact with Gly808 and His810. Remdesivir (Figure S6) maintained the main contacts (Lys50, Asn52, Cys54, and Asp218) except the interaction with Arg116 replaced with polar contacts with Lys74. Analyzing the output of Galidesivir (Figure S7), we observed additional contacts (Arg33, Lys50, and Thr51) with respect to those found by docking calculation (Asn52, Arg116, Lys121, Thr217, and Asp218). Ribavirin was found to maintain all the contacts identified in docking studies during the simulation (Ser343, Asn356, Asn360, Glu370, Val373, Tyr374, Asp377, and Tyr530), although the interaction with Val373 became infrequent (Figure S8). The drug Setrobuvir maintained contacts with Ser835 and Tyr877 during MD experiment, and additionally we observed contacts with Lys807, although mainly water-mediated (Figure S9). Regarding the drug Sofosbuvir by observing the trajectory of MD simulation in addition to the identified contacts (Asn911, Arg914, Tyr915, and Glu919, the latter

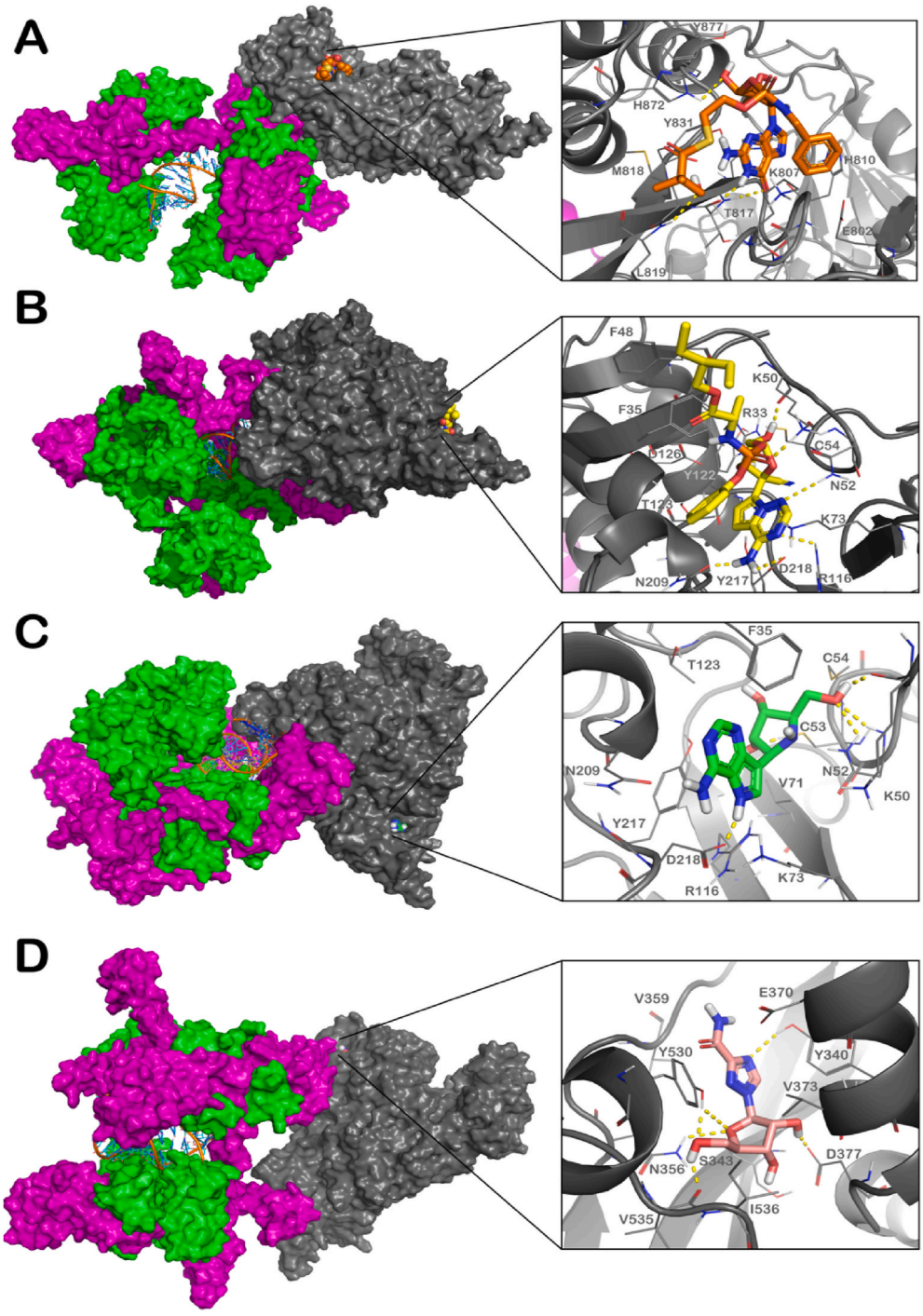


**Fig. 5.** Molecular docking between nsp7-8-12 (nsp7 in green, nsp8 in magenta, nsp12 in gray), viral RNA, and selected antiviral drugs (IDX_184 (panel A), Remdesivir (panel B), Galidesivir (panel C), and Ribavirin (panel D)). Pictures were generated by means of PyMOL.

became mainly water-mediated), we detect additional polar contacts with Glu919 (Figure S10). Tenofovir maintained proficient interactions with Thr120 and Thr123, while the contact with Asp208 became sporadic. We observed two relevant additional contacts with Lys50 and Lys73 (Figure S11). Finally, YAK established a contact with Ala34 that became mainly water-mediated during the simulation. Two additional contacts were observed with Arg33 and Asp208 (Figure S12). In summary, MD simulation studies confirmed the possible binding mode identified for the selected drugs by molecular docking calculation, with only small differences.

Finally, we docked the viral RNA with the selected drug molecules to observe if any of these drugs could bind more tightly to the template RNA strand than that the nsp12-7-8 complex. We observed that the adenine analog Remdesivir bound to RNA most effectively by forming hydrogen bonds and hydrophobic interactions. Hydrogen bonds were observed to be formed between the drug molecule and the nucleotide residues A14(P), U13(P), U16(T), U12(P), U17(T), and A15(P), whereas, hydrophobic interactions were detected with the nucleotide residues of G16(P), C15(T), A19(T), and A18(T). Setrobuvir was also found to effectively bind the viral RNA by forming hydrogen bonds with the nucleotide residues C15(T) and A13(T) of double-stranded RNA and hydrophobic interactions with the nucleotide residues A14(T), A14(P),

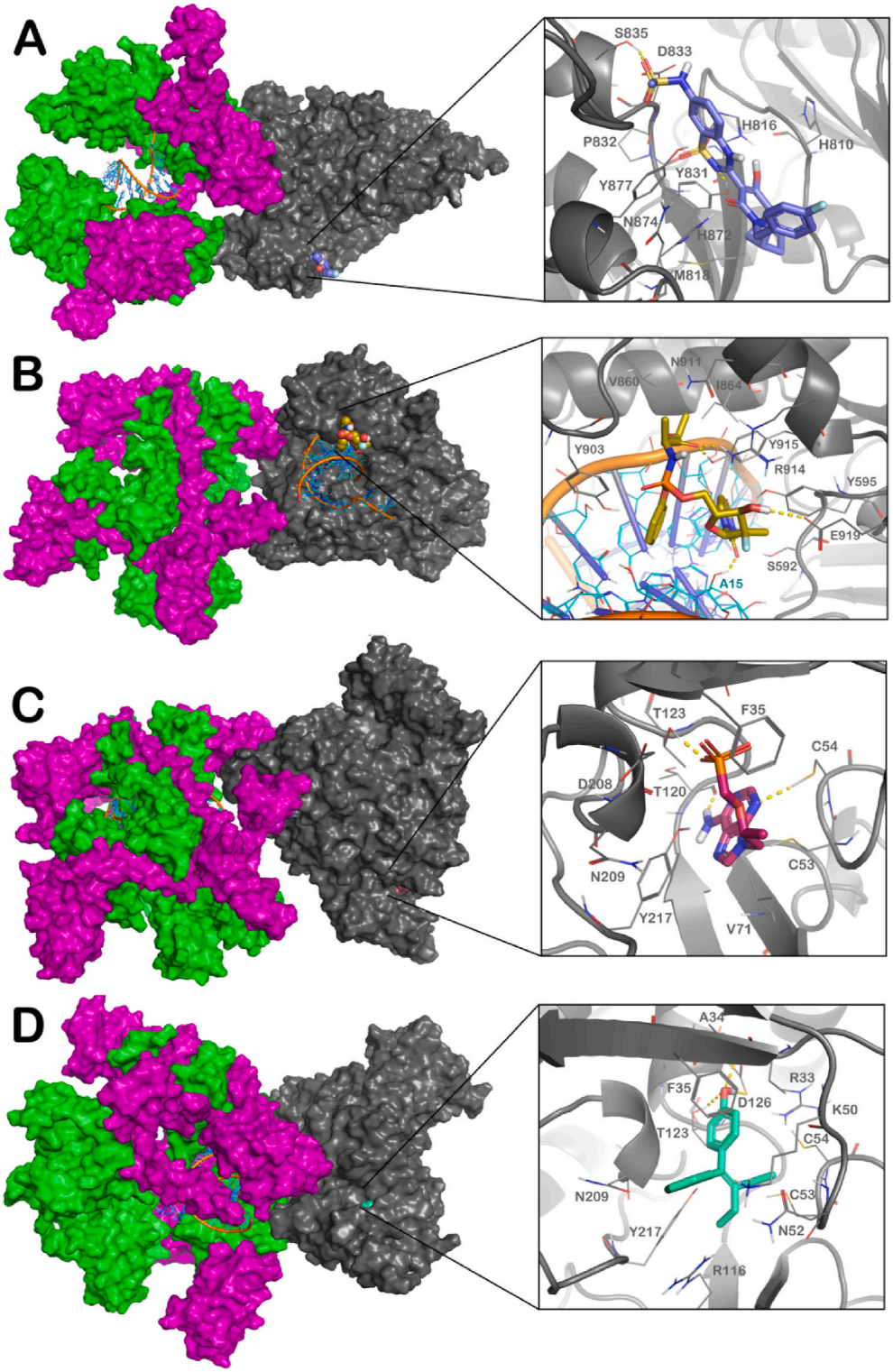


**Fig. 6.** Molecular docking between nsp7-8-12 (nsp7 in green, nsp8 in magenta, nsp12 in gray), viral RNA, and selected antiviral drugs (Setrobuvir (panel A), Sofosbuvir (panel B), Tenofovir (panel C), and YAK (panel D)). Pictures were generated by means of PyMOL.

U10(T), A11(T), A19(P), U12(T), U18(P), and G16(P) (Fig. 8 and Supplementary Table 2). To improve the output of docking calculations of the mentioned complex, we performed a MD simulation (Figure S13). The resulting structure, obtained by molecular docking, was stable with no significant system expansion or contraction. Hydrophobic interactions with template RNA's repetitive nucleotide residues, as well as a lower number of hydrogen bond formations, indicate that Setrobuvir could not bind to the viral RNA as efficiently as Remdesivir. Although the remaining drugs could bind to the viral RNA, they could not bind as strongly as the nsp12-7-8 hexadecameric complex.

This observation implies that the drug Remdesivir could bind to viral RNA strand more effectively than the nsp12-7-8 hexadecameric complex, and as a result, nsp7-8-12 could no longer bind to viral RNA when it is complexed with Remdesivir, as proposed by Yin and colleagues

**Table 4**
Interacting residues of the nsp12-7-8 complex involved in contacts with viral RNA in the absence and presence of drugs, where drugs targeted nsp12 prior to the formation of nsp12-7-8 complex.

| (nsp12 to nsp7-8) to RNA | | (nsp12 with drug) to nsp7-8 to RNA | | | | | | | |
|---|---|---|---|---|---|---|---|---|---|
| | | IDX_184 | | Remdesivir | | Ribavirin | | YAK | |
| Position | Residue | Position | Residue | Position | Residue | Position | Residue | Position | Residue |
| 21 (nsp7) | Arg | 21 (nsp7) | Arg | 31 (nsp7) | Gln | 19 (nsp7) | Gln | 21 (nsp7) | Arg |
| 26 (nsp7) | Ser | 23 (nsp7) | Glu | 54 (nsp7) | Ser | 21 (nsp7) | Arg | 23 (nsp7) | Glu |
| 73 (nsp8) | Gln | 26 (nsp7) | Ser | 57 (nsp7) | Ser | 23 (nsp7) | Glu | 27 (nsp7) | Lys |
| 75 (nsp8) | Arg | 29 (nsp7) | Trp | 61 (nsp8) | Lys | 27 (nsp7) | Lys | 34 (nsp7) | Gln |
| 76 (nsp8) | Ser | 69 (nsp8) | Gln | 65 (nsp8) | Gln | 34 (nsp7) | Gln | 37 (nsp7) | Asn |
| 80 (nsp8) | Arg | 75 (nsp8) | Arg | 406 (nsp12) | Ala | 37 (nsp7) | Asn | 65 (nsp8) | Gln |
| | | | | 408 (nsp12) | Gln | 65 (nsp8) | Gln | 73 (nsp8) | Gln |
| | | | | | | 73 (nsp8) | Gln | 76 (nsp8) | Ser |
| | | | | | | 76 (nsp8) | Ser | 80 (nsp8) | Arg |
| | | | | | | 77 (nsp8) | Glu | 164 (nsp8) | Ser |
| | | | | | | 80 (nsp8) | Arg | | |
| | | | | | | 164 (nsp8) | Ser | | |

| (nsp12 to nsp7-8) to RNA | | (nsp12 with drug) to nsp7-8 to RNA | | | | | | | |
|---|---|---|---|---|---|---|---|---|---|
| | | Galidesivir | | Setrobuvir | | Sofosbuvir | | Tenofovir | |
| Position | Residue | Position | Residue | Position | Residue | Position | Residue | Position | Residue |
| 21 (nsp7) | Arg | 27 (nsp7) | Lys | 21 (nsp7) | Arg | 499 (nsp12) | Asp | 19 (nsp7) | Gln |
| 26 (nsp7) | Ser | 61 (nsp8) | Lys | 24 (nsp7) | Ser | 521 (nsp12) | Tyr | 21 (nsp7) | Arg |
| 73 (nsp8) | Gln | 65 (nsp8) | Gln | 26 (nsp7) | Ser | 814 (nsp12) | Ser | 23 (nsp7) | Glu |
| 75 (nsp8) | Arg | 127 (nsp8) | Lys | 37 (nsp7) | Asn | 903 (nsp12) | Tyr | 30 (nsp7) | Ala |
| 76 (nsp8) | Ser | | | 73 (nsp8) | Gln | | | 37 (nsp7) | Asn |
| 80 (nsp8) | Arg | | | 75 (nsp8) | Arg | | | 80 (nsp8) | Arg |

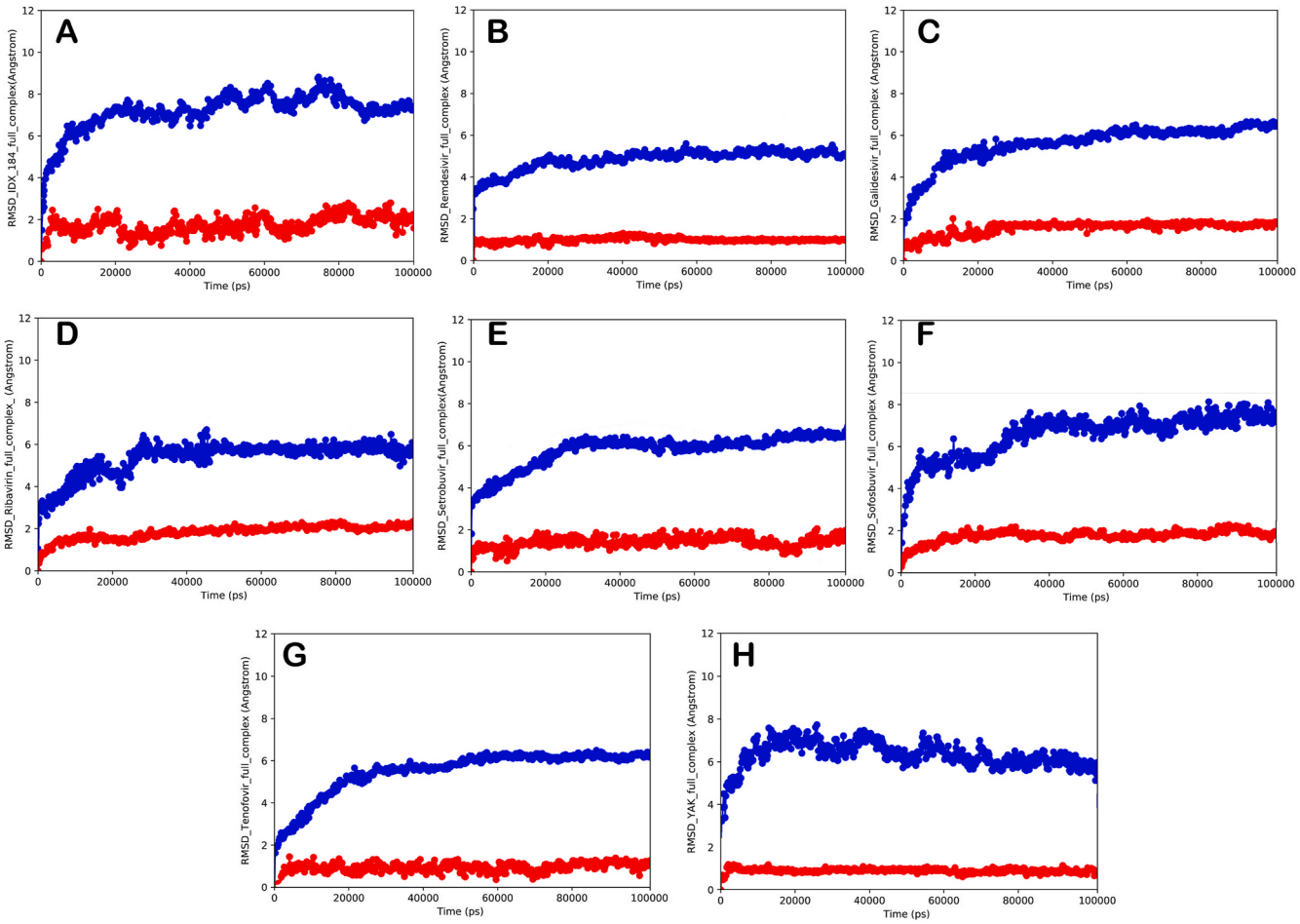


**Fig. 7.** RMSD calculation for each complex enclosing nsp7-8-12 (blue line), viral RNA, and the selected antiviral drugs (red line) (IDX_184 (panel A), Remdesivir (panel B), Galidesivir (panel C), and Ribavirin (panel D), Setrobuvir (panel E), Sofosbuvir (panel F), Tenofovir (panel G), and YAK (panel H)).

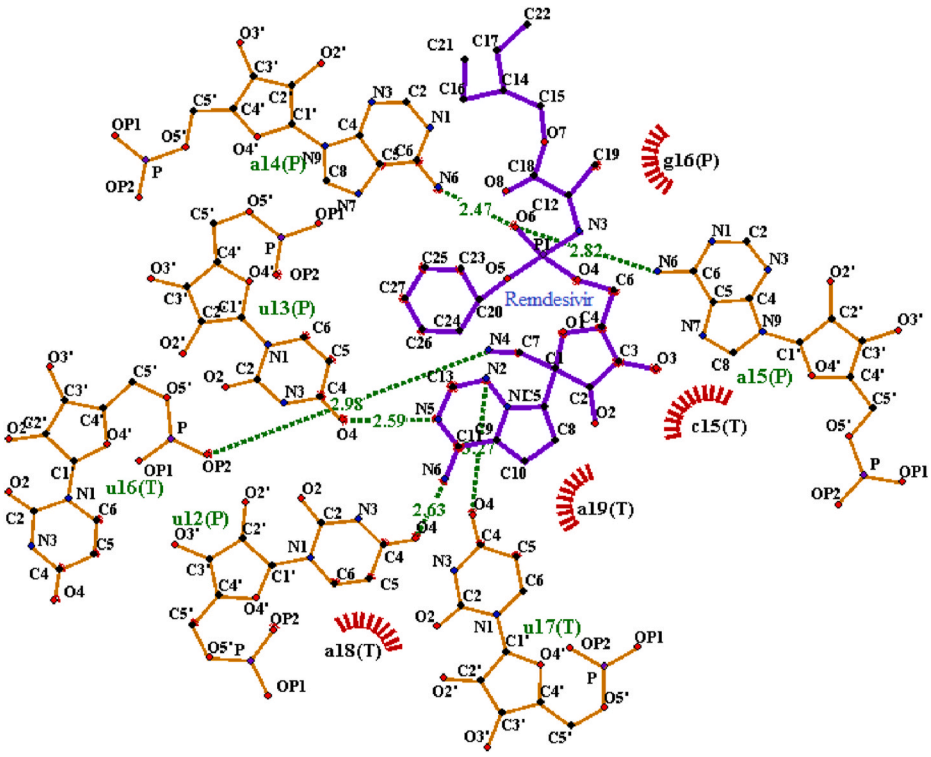


**Fig. 8.** Interaction and interacting sites between the template RNA ("P" and "T" within bracket indicates positive and transcript strand respectively) and Remdesivir visualized through LigPlot + software.

[63]. Furthermore, it is possible to conclude that all other drug molecules are ineffective in inhibiting RdRp-mediated RNA synthesis in the SARS-CoV-2 viral system.

Additionally, the computational experiments yielded 54 unique interaction sites. Except for one site, the multiple alignment analysis (Fig. 9) revealed that these sites are conserved (amino acid number 7 in JalVeiw and position 40 in RdRp). Regarding this position, bat coronavirus_RaTG13/1–7095 and SARS coronavirus have aspartic acid, while other related organisms have glutamic acid. Interestingly, both amino acids belonging to the same group of amino acids (acidic and charged). Because these interacting sites are highly conserved, they can be used to design effective drugs or drug-like molecules in the future. A similar conserved nature of the interacting sites has also been recently described [64].

## 4. Conclusions

These systematic studies demonstrate that SARS-CoV-2 RdRp is more mutable than homologous sequences and evolutionarily close to the bat coronavirus RaTG13, but the sites responsible for the interaction with the cofactor nsp7-8 or with the viral RNA are occupied by identical amino acids. The interactions between RdRp and viral RNA were altered after the drug molecules were incorporated into nsp12, due to the changes in the positions and physico-chemical properties of the interacting amino acids of nsp12. Among the selected existing antiviral drugs, Sofosbuvir was found to be most effective in altering the physico-chemical nature of the interacting amino acids as well as their positions within the RdRp prior to RNA binding. However, when the nsp12 forms a hexadecameric complex with its cofactors, nsp7 and nsp8, none of the drugs affected the physico-chemical nature of the amino acids responsible for interacting with viral RNA or their locations within the nsp12-7-8 complex. Consequently, the selected drugs were unable to bind to the same amino acids of nsp12 when alone. The polymerization activity of the RdRp in SARS-CoV-2 was not hampered, primarily due to the role of cofactors that support the activity of the complex. These findings indicate that special attention must be given to the design of far-reaching drug molecules to nsp12-7-8 hexadecameric structure. Notably, the nucleotide (adenine) analog Remdesivir was more capable to bind with the viral RNA's uracil-rich region than RdRp or to its complex, and thus could prevent RNA chain elongation.

As a result, developing inhibitors that act specifically to reduce viral RNA binding affinity for nsp12 should be prioritized in developing effective antiviral agents against SARS-CoV-2. Furthermore, specific drug molecules with the ability to target residues of the nsp7-8 complex involved in the interaction with nsp12 can be designed to preclude the correct formation of the hexadecameric complex, and thus, reduce the efficiency of RdRp. We have found that Asn69 of nsp7 interacts with Gly897 of nsp12, Cys72 of nsp7 interacts with Gly510 of nsp12, and Glu73 of nsp7 interacts with Arg513 of nsp12. Also, Arg96, Arg111, Asn136, and Met174 of nsp8 interact with Trp509, Leu900, Lys411, and Thr409 of nsp12, respectively, during the formation of the nsp12-7-8 complex. Moreover, two hydrogen bonds were detected between Asn104, and Asn136 of nsp8 and Trp509, and Thr409 of nsp12, respectively. Therefore, blocking these sites of the nsp7/nsp8 complex by specific drug molecules design could change the binding affinity of the nsp7/nsp8 complex to nsp12. Furthermore, drug design targeting the specific sites of the nsp12-7-8 complex responsible for the binding with viral RNA (Arg21, Lys27 of nsp7 and Arg75 and Arg80 of nsp8), may yield fruitful results in blocking the polymerase activity and interrupt the normal life cycle of SARS-CoV-2.

### Compliance with ethical standards

This article does not contain any studies with animals.

### Funding statement

No funding has been received for this work by any author.

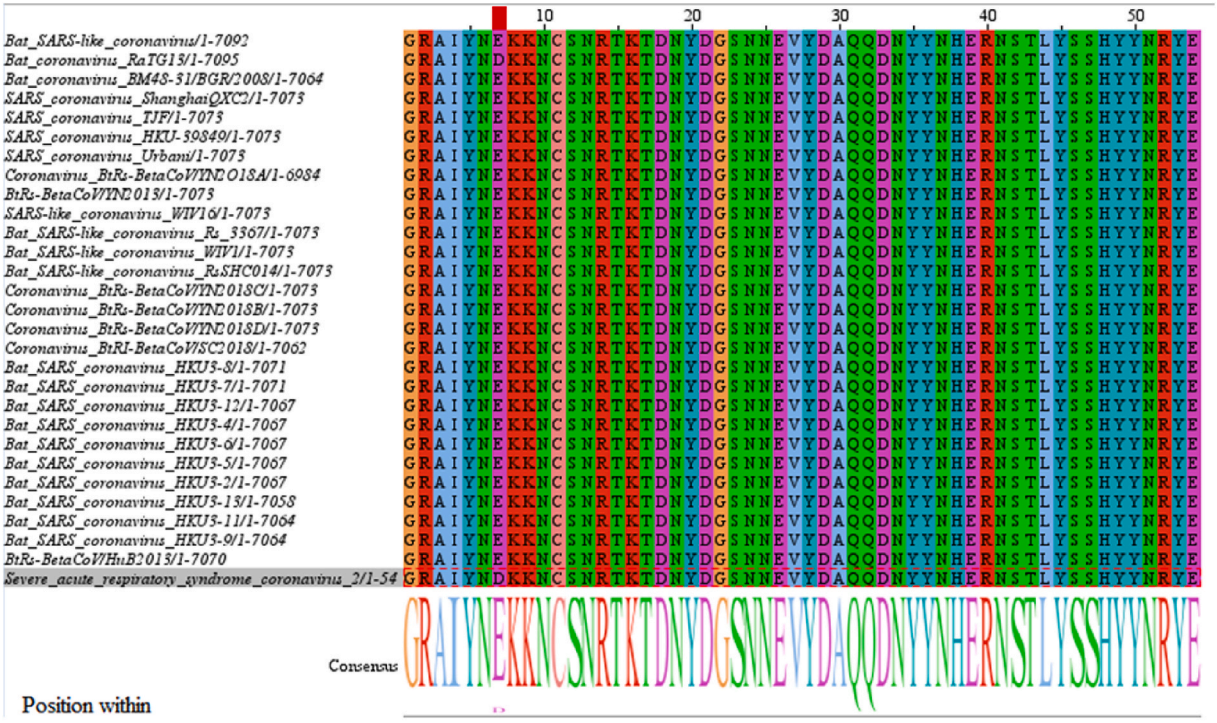


| Jalview | 1 | 2 | 3 | 4 | 5 | 6 | 7 | 8 | 9 | 10 | 11 | 12 | 13 | 14 | 15 | 16 | 17 | 18 |
|---|---|---|---|---|---|---|---|---|---|---|---|---|---|---|---|---|---|---|
| RdRp | 23 | 33 | 34 | 37 | 38 | 39 | 40 | 41 | 50 | 52 | 54 | 78 | 79 | 116 | 120 | 121 | 123 | 208 |
| ORF1ab | 4428 | 4438 | 4439 | 4442 | 4443 | 4444 | 4445 | 4446 | 4455 | 4457 | 4459 | 4483 | 4484 | 4521 | 4525 | 4526 | 4528 | 4613 |
| Jalview | 19 | 20 | 21 | 22 | 23 | 24 | 25 | 26 | 27 | 28 | 29 | 30 | 31 | 32 | 33 | 34 | 35 | 36 |
| RdRp | 209 | 217 | 218 | 220 | 343 | 356 | 360 | 370 | 373 | 374 | 377 | 406 | 408 | 492 | 499 | 507 | 521 | 530 |
| ORF1ab | 4614 | 4622 | 4623 | 4625 | 4748 | 4761 | 4765 | 4775 | 4778 | 4779 | 4782 | 4811 | 4813 | 4897 | 4904 | 4912 | 4926 | 4935 |
| Jalview | 37 | 38 | 39 | 40 | 41 | 42 | 43 | 44 | 45 | 46 | 47 | 48 | 49 | 50 | 51 | 52 | 53 | 54 |
| RdRp | 722 | 725 | 729 | 733 | 734 | 814 | 817 | 819 | 831 | 835 | 861 | 872 | 877 | 903 | 911 | 914 | 915 | 919 |
| ORF1ab | 5127 | 5130 | 5134 | 5138 | 5139 | 5219 | 5222 | 5224 | 5236 | 5240 | 5266 | 5277 | 5282 | 5308 | 5316 | 5319 | 5320 | 5324 |

**Fig. 9.** Interacting sites of RdRp involved in the interaction with RNA and considered drugs.

## Declaration of Competing Interest

There is no conflict of interest.

## Acknowledgments

The authors acknowledge the combined efforts of all scientists in world-wide who are working hard to discover a long-term solution against this pandemic. S.K.M. acknowledges The University of Burdwan for its necessary support. M. K. S. acknowledges the SGS grant (number: 21150/1312/3122) for providing the required infrastructures during the work. The authors also acknowledge, Prof. Chandradipa Ghosh, Prof. Amiya Kumar Panda, Mr. Abhishek Tewari, and Renuka Das for their opinion and valuable suggestions for the preparation of the manuscript. The authors acknowledge Dr. Theresa Ann Reinhardt Piskáčková for English proofreading and revisions.

## Appendix A. Supplementary data

Supplementary data to this article can be found online at https://doi.org/10.1016/j.compbiomed.2021.104591.

## References

[1] C. Bryson-Cahn, J. Duchin, V.A. Makarewicz, M. Kay, K. Rietberg, N. Napolitano, C. Kamangu, T.H. Dellit, J.B. Lynch, A novel approach for a novel pathogen: using a home assessment team to evaluate patients for COVID-19, Clin. Infect. Dis. 71 (2020) 2211–2214.

[2] C. Contini, M. Di Nuzzo, N. Barp, A. Bonazza, R. De Giorgio, M. Tognon, S. Rubino, The novel zoonotic COVID-19 pandemic: an expected global health concern, J Infect Dev Ctries 14 (2020) 254–264.

[3] S.A. Lauer, K.H. Grantz, Q. Bi, F.K. Jones, Q. Zheng, H.R. Meredith, A.S. Azman, N. G. Reich, J. Lessler, The incubation period of coronavirus disease 2019 (COVID-19) from publicly reported confirmed cases: estimation and application, Ann. Intern. Med. 172 (2020) 577–582.

[4] Z.Y. Zu, M.D. Jiang, P.P. Xu, W. Chen, Q.Q. Ni, G.M. Lu, L.J. Zhang, Coronavirus disease 2019 (COVID-19): a perspective from China, Radiology 296 (2020) E15–E25.

[5] A. Sharma, S. Tiwari, M.K. Deb, J.L. Marty, Severe acute respiratory syndrome coronavirus-2 (SARS-CoV-2): a global pandemic and treatment strategies, Int. J. Antimicrob. Agents 56 (2020) 106054.

[6] F. Parvin, S. Islam, Z. Urmy, S. Ahmed, The symptoms, contagious process, prevention and post treatment of covid-19, Eur J Physiother Rehab Studies 1 (2020).

[7] X. Ou, Y. Liu, X. Lei, P. Li, D. Mi, L. Ren, L. Guo, R. Guo, T. Chen, J. Hu, Z. Xiang, Z. Mu, X. Chen, J. Chen, K. Hu, Q. Jin, J. Wang, Z. Qian, Characterization of spike glycoprotein of SARS-CoV-2 on virus entry and its immune cross-reactivity with SARS-CoV, Nat. Commun. 11 (2020) 1620.

[8] E. Tsiambas, V. Papanikolaou, A. Chrysovergis, N. Mastronikolis, V. Ragos, N. Kavantzas, A.C. Lazaris, E. Kyrodimos, Coronavirus in hematologic malignancies: targeting molecules beyond the angiotensin-converting enzyme 2 (ACE2) wall in COVID-19, Pathol. Oncol. Res. 26 (2020) 2823–2825.

[9] S. Kadam, G. Sukhramani, P. Bishnoi, A. Pable, V. Barvkar, Molecular and structural insights into COVID-19 pandemic, in: Preprints.org, 2020.

[10] X. Li, M. Geng, Y. Peng, L. Meng, S. Lu, Molecular immune pathogenesis and diagnosis of COVID-19, J Pharm Anal 10 (2020) 102–108.

[11] M.A. Ullah, Y. Araf, B. Sarkar, A.T. Moin, R.A.I. Reshad, M.D.H. Rahman, Pathogenesis, diagnosis and possible therapeutic options for COVID-19, J Clin Exp Invest 11 (2020), em00755.

[12] Z.W. Ye, S. Yuan, K.S. Yuen, S.Y. Fung, C.P. Chan, D.Y. Jin, Zoonotic origins of human coronaviruses, Int. J. Biol. Sci. 16 (2020) 1686–1697.

[13] S. Perlman, J. Netland, Coronaviruses post-SARS: update on replication and pathogenesis, Nat. Rev. Microbiol. 7 (2009) 439–450.

[14] A.C. Walls, Y.J. Park, M.A. Tortorici, A. Wall, A.T. McGuire, D. Veesler, Structure, function, and antigenicity of the SARS-CoV-2 spike glycoprotein, Cell 181 (2020) 281–292, e286.
[15] A.R. Fehr, S. Perlman, Coronaviruses: an overview of their replication and pathogenesis, Methods Mol. Biol. 1282 (2015) 1–23.
[16] B. Coutard, C. Valle, X. de Lamballerie, B. Canard, N.G. Seidah, E. Decroly, The spike glycoprotein of the new coronavirus 2019-nCoV contains a furin-like cleavage site absent in CoV of the same clade, Antivir. Res. 176 (2020) 104742.
[17] R. Yan, Y. Zhang, Y. Li, L. Xia, Y. Guo, Q. Zhou, Structural basis for the recognition of SARS-CoV-2 by full-length human ACE2, Science 367 (2020) 1444–1448.
[18] P. Zhou, X.L. Yang, X.G. Wang, B. Hu, L. Zhang, W. Zhang, H.R. Si, Y. Zhu, B. Li, C. L. Huang, H.D. Chen, J. Chen, Y. Luo, H. Guo, R.D. Jiang, M.Q. Liu, Y. Chen, X. R. Shen, X. Wang, X.S. Zheng, K. Zhao, Q.J. Chen, F. Deng, L.L. Liu, B. Yan, F. X. Zhan, Y.Y. Wang, G.F. Xiao, Z.L. Shi, A pneumonia outbreak associated with a new coronavirus of probable bat origin, Nature 579 (2020) 270–273.
[19] S. Brogi, V. Calderone, Off-target ACE2 ligands: possible therapeutic option for CoVid-19? Br. J. Clin. Pharmacol. 86 (2020) 1178–1179.
[20] E. Domingo, Molecular basis of genetic variation of viruses, Virus as Populations (2020) 35–71.
[21] A.K. Ah, Z. St, Preprocessing of the candidate antiviral drugs against COVID-19 in models of SARS cov 2 targets, Prensa Med. Argent. 106 (2020).
[22] Y. Gao, L. Yan, Y. Huang, F. Liu, Y. Zhao, L. Cao, T. Wang, Q. Sun, Z. Ming, L. Zhang, J. Ge, L. Zheng, Y. Zhang, H. Wang, Y. Zhu, C. Zhu, T. Hu, T. Hua, B. Zhang, X. Yang, J. Li, H. Yang, Z. Liu, W. Xu, L.W. Guddat, Q. Wang, Z. Lou, Z. Rao, Structure of the RNA-dependent RNA polymerase from COVID-19 virus, Science 368 (2020) 779–782.
[23] K.C. Lehmann, A. Gulyaeva, J.C. Zevenhoven-Dobbe, G.M. Janssen, M. Ruben, H. S. Overkleeft, P.A. van Veelen, D.V. Samborskiy, A.A. Kravchenko, A. M. Leontovich, I.A. Sidorov, E.J. Snijder, C.C. Posthuma, A.E. Gorbalenya, Discovery of an essential nucleotidylating activity associated with a newly delineated conserved domain in the RNA polymerase-containing protein of all nidoviruses, Nucleic Acids Res. 43 (2015) 8416–8434.
[24] C. Huang, Y. Wang, X. Li, L. Ren, J. Zhao, Y. Hu, L. Zhang, G. Fan, J. Xu, X. Gu, Z. Cheng, T. Yu, J. Xia, Y. Wei, W. Wu, X. Xie, W. Yin, H. Li, M. Liu, Y. Xiao, H. Gao, L. Guo, J. Xie, G. Wang, R. Jiang, Z. Gao, Q. Jin, J. Wang, B. Cao, Clinical features of patients infected with 2019 novel coronavirus in Wuhan, China, Lancet 395 (2020) 497–506.
[25] L. Lin, L. Lu, W. Cao, T. Li, Hypothesis for potential pathogenesis of SARS-CoV-2 infection-a review of immune changes in patients with viral pneumonia, Emerg. Microb. Infect. 9 (2020) 727–732.
[26] H. Zhang, J.M. Penninger, Y. Li, N. Zhong, A.S. Slutsky, Angiotensin-converting enzyme 2 (ACE2) as a SARS-CoV-2 receptor: molecular mechanisms and potential therapeutic target, Intensive Care Med. 46 (2020) 586–590.
[27] S.F. Altschul, T.L. Madden, A.A. Schaffer, J. Zhang, Z. Zhang, W. Miller, D. J. Lipman, Gapped BLAST and PSI-BLAST: a new generation of protein database search programs, Nucleic Acids Res. 25 (1997) 3389–3402.
[28] M. Clamp, J. Cuff, S.M. Searle, G.J. Barton, The Jalview Java alignment editor, Bioinformatics 20 (2004) 426–427.
[29] F. Sievers, D.G. Higgins, Clustal omega, Curr Protoc Bioinformatics 48 (2014), 3 13 11-16.
[30] B.G. Hall, Building phylogenetic trees from molecular data with MEGA, Mol. Biol. Evol. 30 (2013) 1229–1235.
[31] S. Kumar, G. Stecher, M. Li, C. Knyaz, K. Tamura, MEGA X: molecular evolutionary genetics analysis across computing platforms, Mol. Biol. Evol. 35 (2018) 1547–1549.
[32] A.A. Elfiky, Ribavirin, remdesivir, Sofosbuvir, Galidesivir, and Tenofovir against SARS-CoV-2 RNA dependent RNA polymerase (RdRp): a molecular docking study, Life Sci. 253 (2020) 117592.
[33] A.A. Elfiky, SARS-CoV-2 RNA dependent RNA polymerase (RdRp) targeting: an in silico perspective, J. Biomol. Struct. Dyn. (2020) 1–9.
[34] S. Brogi, A. Ramunno, L. Savi, G. Chemi, G. Alfano, A. Pecorelli, E. Pambianchi, P. Galatello, G. Compagnoni, F. Focher, G. Biamonti, G. Valacchi, S. Butini, S. Gemma, G. Campiani, M. Brindisi, First dual AK/GSK-3 beta inhibitors endowed with antioxidant properties as multifunctional, potential neuroprotective agents, Eur. J. Med. Chem. 138 (2017) 438–457.
[35] A. Reale, S. Brogi, A. Chelini, M. Paolino, A. Di Capua, G. Giuliani, A. Cappelli, G. Giorgi, G. Chemi, A. Grillo, M. Valoti, L. Sautebin, A. Rossi, S. Pace, C. La Motta, L. Di Cesare Mannelli, E. Lucarini, C. Ghelardini, M. Anzini, Synthesis, biological evaluation and molecular modeling of novel selective COX-2 inhibitors: sulfide, sulfoxide, and sulfone derivatives of 1,5-diarylpyrrol-3-substituted scaffold, Bioorg. Med. Chem. 27 (2019) 115045.
[36] M. Brindisi, C. Ulivieri, G. Alfano, S. Gemma, F. de Asis Balaguer, T. Khan, A. Grillo, G. Chemi, G. Menchon, A.E. Prota, N. Olieric, D. Lucena-Agell, I. Barasoain, J.F. Diaz, A. Nebbioso, M. Conte, L. Lopresti, S. Magnano, R. Amet, P. Kinsella, D.M. Zisterer, O. Ibrahim, J. O'Sullivan, L. Morbidelli, R. Spaccapelo, C. Baldari, S. Butini, E. Novellino, G. Campiani, L. Altucci, M.O. Steinmetz, S. Brogi, Structure-activity relationships, biological evaluation and structural studies of novel pyrrolonaphthoxazepines as antitumor agents, Eur. J. Med. Chem. 162 (2019) 290–320.
[37] H. Sirous, G. Chemi, G. Campiani, S. Brogi, An integrated in silico screening strategy for identifying promising disruptors of p53-MDM2 interaction, Comput. Biol. Chem. 83 (2019) 107105.
[38] H. Sirous, G. Chemi, S. Gemma, S. Butini, Z. Debyser, F. Christ, L. Saghaie, S. Brogi, A. Fassihi, G. Campiani, M. Brindisi, Identification of novel 3-Hydroxy-pyran-4-One derivatives as potent HIV-1 integrase inhibitors using in silico structure-based combinatorial library design approach, Front Chem 7 (2019) 574.
[39] C.J. Williams, J.J. Headd, N.W. Moriarty, M.G. Prisant, L.L. Videau, L.N. Deis, V. Verma, D.A. Keedy, B.J. Hintze, V.B. Chen, S. Jain, S.M. Lewis, W. B. Arendall 3rd, J. Snoeyink, P.D. Adams, S.C. Lovell, J.S. Richardson, D. C. Richardson, MolProbity: more and better reference data for improved all-atom structure validation, Protein Sci. 27 (2018) 293–315.
[40] R. Luthy, J.U. Bowie, D. Eisenberg, Assessment of protein models with three-dimensional profiles, Nature 356 (1992) 83–85.
[41] Y. Yan, D. Zhang, P. Zhou, B. Li, S.Y. Huang, HDOCK: a web server for protein-protein and protein-DNA/RNA docking based on a hybrid strategy, Nucleic Acids Res. 45 (2017) W365–W373.
[42] A.C. Wallace, R.A. Laskowski, J.M. Thornton, LIGPLOT: a program to generate schematic diagrams of protein-ligand interactions, Protein Eng. 8 (1995) 127–134.
[43] E.F. Pettersen, T.D. Goddard, C.C. Huang, G.S. Couch, D.M. Greenblatt, E.C. Meng, T.E. Ferrin, UCSF Chimera–a visualization system for exploratory research and analysis, J. Comput. Chem. 25 (2004) 1605–1612.
[44] S. Salentin, S. Schreiber, V.J. Haupt, M.F. Adasme, M. Schroeder, PLIP: fully automated protein-ligand interaction profiler, Nucleic Acids Res. 43 (2015) W443–W447.
[45] J. Nickolls, I. Buck, M. Garland, K. Skadron, Scalable parallel programming with CUDA, Queue 6 (2008) 40.
[46] W.L. Jorgensen, J. Chandrasekhar, J.D. Madura, R.W. Impey, M.L. Klein, Comparison of simple potential functions for simulating liquid water, J. Chem. Phys. 79 (1983) 926–935.
[47] W.L. Jorgensen, D.S. Maxwell, J. Tirado-Rives, Development and testing of the OPLS all-atom force field on conformational energetics and properties of organic liquids, J. Am. Chem. Soc. 118 (1996) 11225–11236.
[48] S. Brogi, S. Butini, S. Maramai, R. Colombo, L. Verga, C. Lanni, E. De Lorenzi, S. Lamponi, M. Andreassi, M. Bartolini, V. Andrisano, E. Novellino, G. Campiani, M. Brindisi, S. Gemma, Disease-modifying anti-Alzheimer's drugs: inhibitors of human cholinesterases interfering with beta-amyloid aggregation, CNS Neurosci. Ther. 20 (2014) 624–632.
[49] H. Sirous, A. Fassihi, S. Brogi, G. Campiani, F. Christ, Z. Debyser, S. Gemma, S. Butini, G. Chemi, A. Grillo, R. Zabihollahi, M.R. Aghasadeghi, L. Saghaie, H. R. Memarian, Synthesis, molecular modelling and biological studies of 3-hydrox-ypyrane- 4-one and 3-hydroxy-pyridine-4-one derivatives as HIV-1 integrase inhibitors, Med. Chem. 15 (2019) 755–770.
[50] D.D. Humphreys, R.A. Friesner, B.J. Berne, A multiple-time-step molecular dynamics algorithm for macromolecules, J. Phys. Chem. 98 (1994) 6885–6892.
[51] W.G. Hoover, Canonical dynamics: equilibrium phase-space distributions, Phys. Rev. 31 (1985) 1695–1697.
[52] G.J. Martyna, D.J. Tobias, M.L. Klein, Constant pressure molecular dynamics algorithms, J. Chem. Phys. 101 (1994) 4177–4189.
[53] U. Essmann, L. Perera, M.L. Berkowitz, T. Darden, H. Lee, L.G. Pedersen, A smooth particle mesh Ewald method, J. Chem. Phys. 103 (1995) 8577–8593.
[54] E.B. Ludmir, L.W. Enquist, Viral genomes are part of the phylogenetic tree of life, Nat. Rev. Microbiol. 7 (2009) 615, author reply 615.
[55] X. Chen, Understanding the development and perception of global health for more effective student education, Yale J. Biol. Med. 87 (2014) 231–240.
[56] B.D. Rife, C. Mavian, X. Chen, M. Ciccozzi, M. Salemi, J. Min, M.C. Prosperi, Phylodynamic applications in 21(st) century global infectious disease research, Glob Health Res Policy 2 (2017) 13.
[57] R. Matyasek, A. Kovarik, Mutation Patterns of Human SARS-CoV-2 and Bat RaTG13 Coronavirus Genomes Are Strongly Biased towards C>U Transitions, Indicating Rapid Evolution in Their Hosts, Genes (Basel), 2020, p. 11.
[58] J. Lu, J. Cui, Z. Qian, Y. Wang, H. Zhang, Y. Duan, X. Wu, X. Yao, Y. Song, X. Li, C. Wu, X. Tang, On the origin and continuing evolution of SARS-CoV-2, Natl Sci Rev 7 (2020) 1012–1023.
[59] A.J. te Velthuis, S.H. van den Worm, E.J. Snijder, The SARS-coronavirus nsp7+ nsp8 complex is a unique multimeric RNA polymerase capable of both de novo initiation and primer extension, Nucleic Acids Res. 40 (2012) 1737–1747.
[60] H.S. Hillen, G. Kokic, L. Farnung, C. Dienemann, D. Tegunov, P. Cramer, Structure of replicating SARS-CoV-2 polymerase, Nature 584 (2020) 154–156.
[61] K. Barakat, M. Ahmed, Y. Tabana, M. Ha, A "Deep Dive" into the SARS-Cov-2 Polymerase Assembly: Identifying Novel Allosteric Sites and Analyzing the Hydrogen Bond Networks and Correlated Dynamics, bioRxiv, 2020, 2020.2006.2002.130849.
[62] S. Brogi, H. Sirous, V. Calderone, G. Chemi, Amyloid beta fibril disruption by oleuropein aglycone: long-time molecular dynamics simulation to gain insight into the mechanism of action of this polyphenol from extra virgin olive oil, Food Funct 11 (2020) 8122–8132.
[63] W. Yin, C. Mao, X. Luan, D.D. Shen, Q. Shen, H. Su, X. Wang, F. Zhou, W. Zhao, M. Gao, S. Chang, Y.C. Xie, G. Tian, H.W. Jiang, S.C. Tao, J. Shen, Y. Jiang, H. Jiang, Y. Xu, S. Zhang, Y. Zhang, H.E. Xu, Structural basis for inhibition of the RNA-dependent RNA polymerase from SARS-CoV-2 by remdesivir, Science 368 (2020) 1499–1504.
[64] R. Jacome, J.A. Campillo-Balderas, S. Ponce de Leon, A. Becerra, A. Lazcano, Sofosbuvir as a potential alternative to treat the SARS-CoV-2 epidemic, Sci. Rep. 10 (2020) 9294.